Controlling the crystal packing and morphology of metal–organic macrocycles through side-chain modification

Leo B. Zasada,[†] Phuong H. Le,[†] Audrey M. Hill,[†] Ryan T. Shafranek,[†] and Dianne J. Xiao[†,*]

[†] Department of Chemistry, University of Washington, Seattle, Washington 98195, United States
* Corresponding author: djxiao@uw.edu

Abstract: Supramolecular nanotubes constructed from the self-assembly of conjugated metal–organic macrocycles provide a unique collection of materials properties, including solution processability, porosity, and electrical conductivity. Here we show how small modifications to the macrocycle periphery subtly alter the noncovalent interactions governing self-assembly, leading to large changes in crystal packing, crystal morphology, and materials properties. Specifically, we synthesized five distinct copper-based macrocycles that differ in either the steric bulk, polarity, or hydrogen-bonding ability of the peripheral side-chains. We show that increased steric bulk leads to more disordered π–π stacking and lower electrical conductivity, whereas hydrogen-bonding groups lead to more ordered intermolecular interactions and a dramatic increase in crystallite size. Together, these results establish side-chain engineering as a rich toolkit for controlling the packing structure, particle morphology, and bulk properties of conjugated metal–organic macrocycles.

Introduction.

Large macrocycles that self-assemble into extended nanotubular structures provide a fertile middle ground in between molecules and materials.[1–5] As molecules, macrocycles offer processability along with the ability to tune chemical structure with atomic precision. As materials, they possess multifunctional pore channels that can be used to mimic biological water channels,[6] selectively transport molecules,[7,8] conduct ions,[9–12] and host chemical reactions.[13,14] In addition, because the supramolecular architectures are held together by weak noncovalent interactions, these self-assembled nanotubes provide dynamic and stimuli-responsive properties.[15,16]

We have been interested in macrocyclic motifs that mimic the structures of conjugated 2D metal–organic frameworks (MOFs) and covalent organic frameworks (COFs) (**Fig. 1**).[17] Such macrocycles should couple the benefits of supramolecular polymers (e.g., processability, stimuli-responsiveness, self-healing properties)[18–20] with the unique electronic properties of semiconducting framework materials. Indeed, we have shown that fully conjugated copper-based macrocycles preserve the porosity and electrical conductivity of conjugated 2D MOFs while offering significant processability advantages.[17]

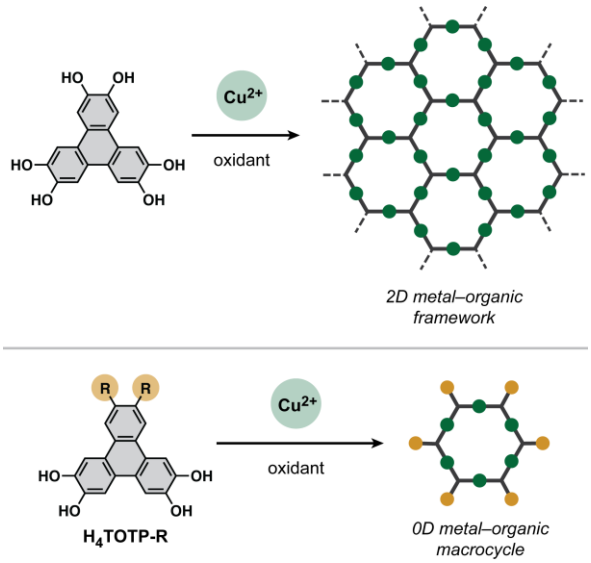

Fig. 1 | Overview of the synthesis and structure of conjugated 2D metal–organic frameworks *(top)* and conjugated metal–organic macrocycles *(bottom)*. The tunable peripheral side chains (R) are highlighted in yellow.

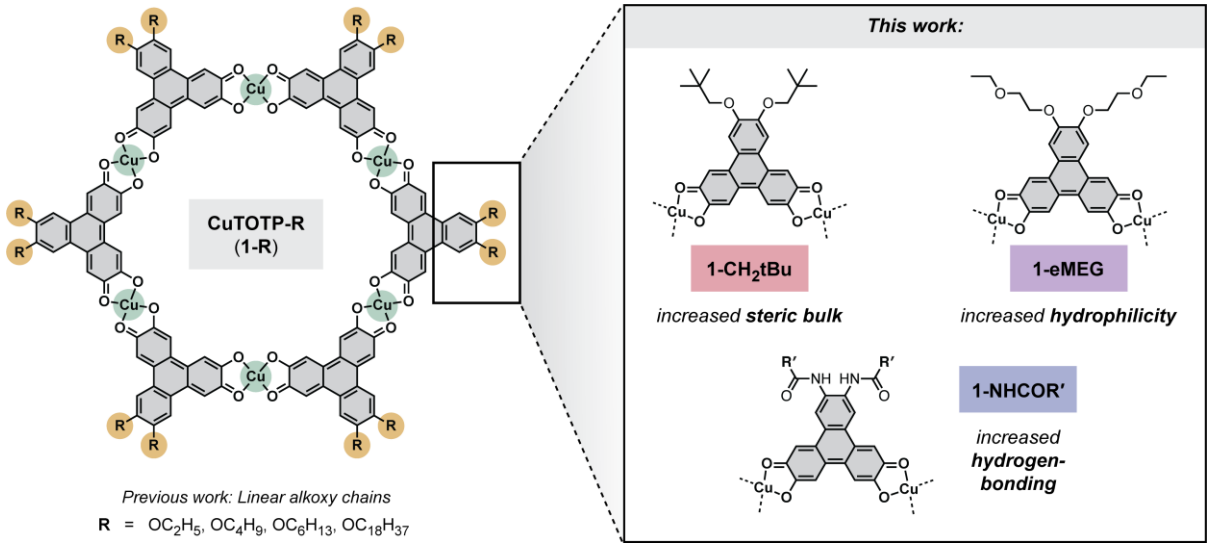

Fig. 2 | Overview of side-chain modifications in the macrocycle CuTOTP-R (**1-R**). Previous work investigated linear alkoxy side-chains of varying lengths (C2, C4, C6, and C18). In this work, we explore the effects of increased steric bulk, hydrophilicity, and hydrogen-bonding on crystal packing, crystal morphology, and materials properties.

In our previous work, only linear alkoxy side-chains of varying lengths (linear C2, C4, C6, and C18) were explored. As supramolecular self-assembly is highly sensitive to molecular structure, we hypothesized that changes to the macrocycle periphery should profoundly impact the underlying π–π stacking structure and bulk materials properties, as well as the crystallization process and overall particle morphology.

To explore how the chemical identity of the peripheral side-chain impacts nanotube self-assembly, we synthesized five distinct copper macrocycles functionalized with either 1) sterically bulky branched alkoxy substituents, 2) hydrophilic ethylene glycol derivatives, or 3) hydrogen-bonding amide groups of varying chain lengths (**Fig. 2**). We show that increased steric bulk leads to more disordered π–π stacking and lower electrical conductivity, while hydrogen-bonding groups lead to more ordered intermolecular interactions and a dramatic increase in average particle size. Together, these results illustrate how side-chain engineering can be a powerful tool to modulate the underlying structure and bulk properties of conjugated metal–organic macrocycles.

Results and discussion.

Ligand synthesis. Sterically bulky and hydrophilic side-chains could be installed on substituted 2,3,6,7-tetrahydroxytriphenylene ligands (H_4TOTP-R) via minor adjustments to the original synthesis route (**Scheme 1a**).[17,21] In our previous work, we showed that linear alkoxy chains of varying lengths (R = OC2, OC4, OC6, and OC18) could be easily attached to the ligand periphery via nucleophilic substitution. In a similar fashion, sterically bulky and hydrophilic and side-chains can be installed by reacting the starting 4,5-dibromo-1,2-diol with either neopentyl tosylate or 2-ethoxyethyl methanesulfonate, respectively. The final ligands H_4TOTP-OCH_2tBu and H_4TOTP-eMEG (eMEG = ethyl-capped monoethylene glycol) were obtained after Suzuki coupling, Scholl cyclization, and silyl protecting group removal (**Scheme 1a**; see Supporting Information for full experimental details).

In contrast, significant modifications to the original synthetic route were needed to achieve amide-functionalized ligands (**Scheme 1b**). Rather than using a catechol-based starting material, we began with synthesizing *tert*-butyloxycarbonyl (BOC) protected 4,5-dibromobenzene-1,2-diamine. Subsequent Suzuki coupling, Scholl cyclization, and BOC deprotection generates intermediate **Int-1**, which can be treated with acyl chlorides to form the desired amide bond. The final ligands H_4TOTP-NHCOR′ (R′ = linear C2, C4, or C6 alkyl chains) were obtained after silyl protecting group removal (see Supporting Information for full experimental details). In principle, intermediate **Int-1** should be able to react with diverse electrophiles beyond acyl chlorides, providing an opportunity for late-stage ligand diversification.

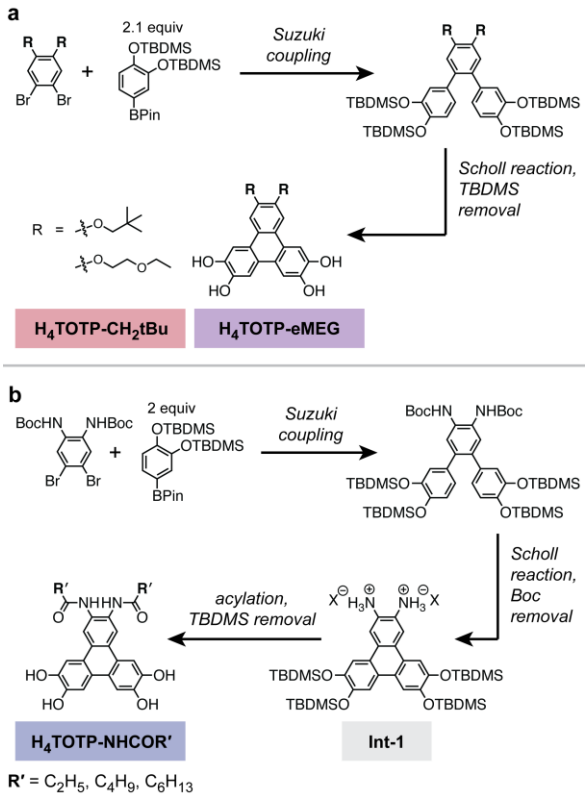

Scheme 1 | Synthetic routes to obtain (a) sterically bulky H_4TOTP-OCH$_2$tBu and hydrophilic H_4TOTP-eMEG ligands, as well as (b) amide-functionalized H_4TOTP-NHCOR′ ligands.

Impact of steric bulk and polarity on crystal packing. Both the neopentoxy and eMEG-functionalized copper macrocycles were readily isolated as dark blue-black solids by combining $Cu(OAc)_2 \cdot H_2O$ and the ligand H_4TOTP-R (R = OCH$_2$tBu or eMEG) in a mixture of DMF and a cosolvent in air at room temperaure. Methanol and mesitylene were used as the cosolvents for CuTOTP-OCH$_2$tBu (abbreviated **1-OCH$_2$tBu**) and CuTOTP-eMEG (abbreviated **1-eMEG**), respectively (see SI for more synthetic details).

Powder X-ray diffraction (PXRD) was used to probe how the presence of bulky neopentyl groups in **1-OCH$_2$tBu** influenced macrocycle packing (**Fig. 3a**). The positions of the first three peaks in the PXRD are consistent with a hexagonal unit cell ($a = b = 38.8$ Å), indicating that the macrocycles are still able to form columnar stacking structures. However, in contrast to our previously reported macrocycles, no distinct π–π stacking feature could be observed in **1-OCH$_2$tBu**. This suggests that the neopentyl groups introduce significant disorder in the π–π stacking distance and geometry. Furthermore, pressed pellet conductivity measurements show that these disruptions to the π–π stacking greatly hinder out-of-plane charge transport. Despite being similar in size to the ethoxy-functionalized macrocycle CuTOTP-OC2 ($a = b = 39.6$ Å), **1-OCH$_2$tBu** is nearly three orders of magnitude less conductive ($2(1) \times 10^{-3}$ vs. $6(2) \times 10^{-6}$ S/cm).[17]

The addition of hydrophilic oligoethylene glycol side chains has been shown to endow polythiophene and other traditional semiconducting polymers with greater ionic conductivity.[22,23] Such mixed ionic-electronic conductors have attracted strong recent interest due to emerging applications in bioelectronic, optoelectronic, and energy storage devices.[24,25] Given this prior work, we were interested in how the addition of a simple ethylene glycol derivative impacts macrocycle formation and packing.

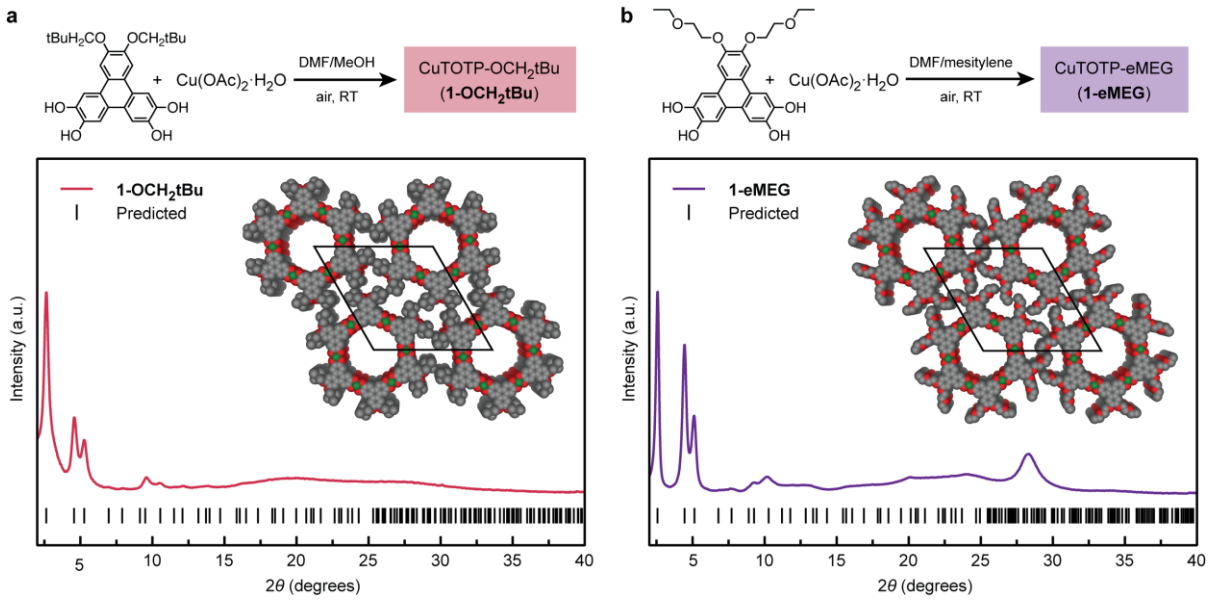

Fig. 3 | Synthesis schemes, experimental and predicted powder X-ray diffraction patterns, and structural models for (a) CuTOTP-OCH$_2$tBu (**1-CH$_2$tBu**) and (b) CuTOTP-eMEG (**1-eMEG**).

Excitingly, in contrast to **1-OCH$_2$tBu**, the polar side-chains of **1-eMEG** do not appear to disrupt the π–π stacking (**Fig. 3b**). A strong π–π stacking feature at 2θ = 28.3° is observed, corresponding to a distance of ~3.2 Å. Consistent with this observation, pressed pellet conductivity measurements show that these macrocycles maintain a moderate electrical conductivity of 5(1) × 10^{-4} S/cm. Interestingly, the *a* and *b* dimensions of **1-eMEG** are only 1.3 Å larger than our previously reported CuTOTP-OC2 (39.8 Å vs. 38.5 Å), despite having a side-chain that is twice as long.[17] This may be due to the tendency of glycol side-chains to curl and bend, in contrast to the linear conformations preferred by *n*-alkyl chains.[26] Together, these results suggest that hydrophilic side-chains do not interfere with macrocycle packing, encouraging future work exploring mixed ionic-electronic conductivity in these materials.

Impact of hydrogen-bonding interactions on crystal packing. The addition of hydrogen-bonding amide groups has been shown to enforce columnar stacking in shape-persistent arylene ethynylene macrocycles, enabling their self-assembly into long nanotube filaments.[10,27] In a similar way, we hypothesized that hydrogen-bonding amide groups could introduce stronger and more directional noncovalent interactions between neighboring macrocycles, facilitating the crystallization of larger particles.

The macrocycles **1-NHCOR′** (R′ = linear C2, C4, or C6 alkyl chains) were readily synthesized by combining the ligand H$_4$TOTP-NHCOR′ with Cu(OAc)$_2$·H$_2$O in DMSO at room temperature in air. Unexpectedly, the PXRD patterns of all three macrocycles (R′ = C2, C4, C6) reveal a complex pattern that could not be indexed to a single unit cell, suggesting a mixture of phases (**Fig. 4a**). The presence of prominent peaks with the characteristic 1:1/√3:1/2 d-spacing ratio for a hexagonal unit cell (e.g., 2θ = 2.54, 4.42, and 5.30° for **1-NHCOC4**) suggests that these samples contain a mixture of hexagonal packing and a second, unknown packing structure.

Partial or total conversion to a single hexagonal phase occurs upon solvent removal at room temperature, implying that the additional crystalline phases are due to alternative macrocyclic packing motifs rather than structurally distinct linear polymers or partially cyclized oligomers (**Fig. 4b**). For example, while the initially filtered samples of **1-NHCOC2** and **1-NHCOC4** both show

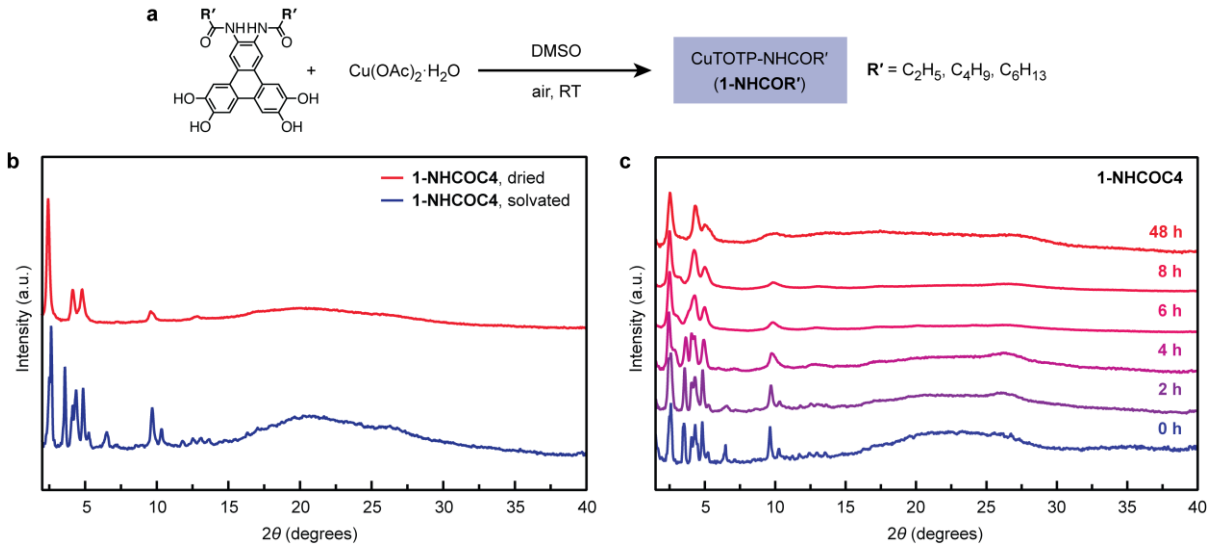

Fig. 4 | (a) Synthesis of CuTOTP-NHCOR′ (**1-NHCOR′**) macrocycles. (b) Powder X-ray diffraction (PXRD) of as-synthesized and dried **1-NHCOC4** in blue and red, respectively. The as-synthesized sample contains a mixture of phases, whereas the dried sample is a single hexagonal phase. (c) PXRD patterns tracking the phase conversion of the as-synthesized **1-NHCOC4** macrocycle over a period of 48 hours.

a mixture of phases, complete conversion to a single hexagonal phase is observed after air-drying at room temperature (**Fig. 4** and **Fig. S7**). This process can be reversed through the re-addition of DMSO (**Fig. S1**), again implying that these structural changes are due to the reconfiguration of dynamic noncovalent interactions rather than stronger metal–ligand bonds. We note that only partial conversion is observed for **1-NHCOC6** (**Fig. S7**).

As expected, the electrical conductivity of **1-NHCOR′** decreases as the length of the insulating alkyl chain increases. The room temperature pressed pellet conductivity of **1-NHCOC2** is $2(1) \times 10^{-3}$ S/cm, whereas the longer **1-NHCOC4** is an order of magnitude lower, at $2(1) \times 10^{-4}$ S/cm. Surprisingly, the conductivity of a mixed-phase **1-NHCOC4** sample was within error of the pure hexagonal phase, at $8(4) \times 10^{-5}$ S/cm. Similarly, the mixed-phase **1-NHCOC6** was only slightly lower, at $5(2) \times 10^{-5}$ S/cm. These values suggest that the additional phase(s) likely preserve strong π-overlap between neighboring macrocycles.

Given the complexity of the initial PXRD patterns, structural elucidation of the non-hexagonal phase(s) will likely require single crystal diffraction studies. Unfortunately, the crystallites were too small for single crystal X-ray diffraction, and all attempts at electron diffraction were unsuccessful due to rapid degradation upon removal from the mother liquor. However, modeling studies suggest that the additional peaks cannot be explained by either herringbone packing (**Fig. S2**) or slipped stacking (**Fig. S3**), which are two of the most common packing motifs observed in the solid-state structures of conjugated organic molecules (see SI for more modeling details).[28]

Impact of hydrogen-bonding interactions on crystal morphology. Excitingly, all three amide-containing macrocycles formed large, micron-sized particles that could be visualized by optical microscopy (**Fig. 5** and **Fig. S4**). This is in stark contrast to **1-OCH$_2$tBu**, **1-eMEG**, and our previously reported alkoxy-functionalized macrocycles, which precipitate as nanoparticles that are challenging to visualize by either optical or scanning electron microscopy (SEM). For example, AFM measurements on CuTOTP-OC4 showed that the columnar stacks have an average length of only 23(6) nm.[17]

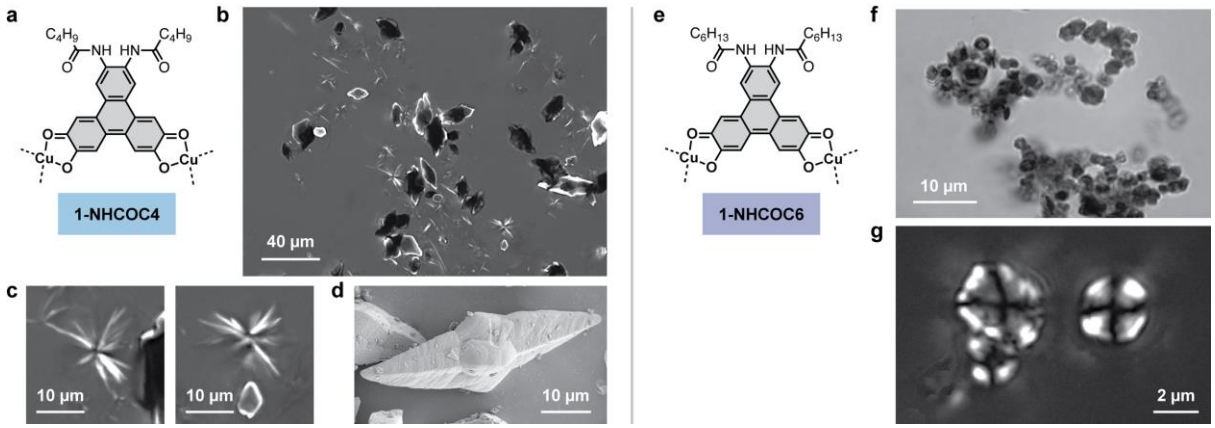

Fig. 5 | *Left:* (a) Chemical structure and (b) polarized optical microscopy image of **1-NHCOC4**. Both thin, aggregated microneedles and thick, irregular octahedra are observed. Zoomed-in (c) polarized optical microscopy and (d) scanning electron microscopy (SEM) images of the two particle morphologies. *Right:* (e) Chemical structure and (f) bright-field optical microscopy image of **1-NHCOC6**, which adopts a spherulite morphology. (g) Polarized optical microscopy image showing the Maltese cross pattern characteristic of spherulites.

The macrocycle **1-NHCOC2** formed aggregated clusters that were challenging to fully resolve by optical microscopy (**Fig. S4**). In contrast, **1-NHCOC4** formed large and well-defined particles. Two distinct crystal morphologies could be clearly visualized in **1-NHCOC4**, supporting our hypothesis that the as-synthesized sample contains two distinct phases (**Fig. 5b**). Specifically, both aggregates of thin microneedles (~6(3) µm average length) (**Fig. 5c** and **Fig. S12**) as well as thick, irregular octahedra (~27(11) µm average length) were observed (**Fig. 5d** and **Fig. S12**). The larger octahedral particles could be removed by gentle centrifugation. Powder X-ray diffraction measurements on the particles suspended in the supernatant confirmed that the smaller needle-like crystals are pure hexagonal phase material (**Fig. S5**). Imaging the samples under polarized light confirmed that the individual microneedles were single crystalline, whereas the larger distorted octahedra grew overall microcrystalline. This is consistent with our PXRD studies, which showed that the non-hexagonal phase is highly sensitive to phase transitions (**Fig. 4c**) which may prevent long-range order.

Finally, **1-NHCOC6** crystallizes as spherulites of approximately 2.6(0.5) µm in diameter (**Fig. 5f** and **Fig. S12**). Spherulites are densely packed spheres composed of radially oriented fibrillar crystals, which display a characteristic Maltese cross when viewed between crossed polarizers (**Fig. 5g**).[29] The formation of spherulites, rather than well-defined needles, may be due to the presence of longer alkyl chains in **1-NHCOC6** that are poorly soluble in DMSO, our reaction solvent.

Overall, the crystal morphologies of **1-NHCOR′** strongly resemble those of conjugated 2D MOFs, such as $Cu_3(HHTP)_2$. Like our macrocycles, the framework $Cu_3(HHTP)_2$ typically crystallizes as thin rods or needles with the π-stacking direction oriented along the long axis.[30,31] In addition, conditions of rapid nucleation produce spherical clusters of radially oriented nanorods,[32] much like the aggregated microneedles found in **1-NHCOC4** and the spherulites in **1-NHCOC6**. Importantly, this suggests that understanding how to control the nucleation and growth of conjugated macrocycles may lead to a greater understanding of the formation of conjugated metal–organic frameworks, and vice versa.

Conclusion.

In conclusion, we have synthesized five new conjugated metal–organic macrocycles containing side-chains that vary in their steric bulk, hydrophilicity, and hydrogen-bonding ability. Despite the chemically distinct peripheral functionalities, all ligands successfully form macrocyclic structures, illustrating the versatility and robustness of this synthetic route. While the conjugated core is reminiscent of 2D metal–organic frameworks, the peripheral side-chains are a unique feature of macrocycles, and represent an exciting opportunity to tailor materials properties. We have already shown how the side-chains can be used to alter the π–π stacking structure, electrical conductivity, crystal morphology, and overall processability of these materials. Going forward, the peripheral side-chains have the potential to introduce hydrophilicity and ionic conductivity, as well as modulate the local microenvironment and reactivity of the metal center.

Finally, a key finding from our studies is that the introduction of stronger and more directional hydrogen-bonding interactions in the π-stacking direction leads to a dramatic increase in particle size, from the nano- to the micron scale. Given the structural similarities between our macrocycles and conjugated 2D metal–organic frameworks, this finding may have implications in the crystallization and growth of 2D MOFs. The new ligand synthesis route reported here readily accommodates the late-stage installation of diverse hydrogen-bonding groups, encouraging future work along this vein.

Experimental Methods.

All the ligand syntheses, macrocycle syntheses, and phase conversions are described in detail in the Supplementary Information. Powder X-ray diffraction patterns were collected on a Bruker D8 Discover diffractometer. Solution phase NMR data were collected on Bruker GG500 or NEO500 instruments. Optical microscopy images were collected on a Leica DMI6000 inverted microscope using oil immersion objectives, and images were analyzed in LASX (Leica) and ImageJ. SEM images were collected on a Thermo Fisher Scientific Apreo-S with LoVac scanning electron microscope with an operating voltage of 2 kV.

Acknowledgements.

This material is based upon work supported by the U.S. Department of Energy, Office of Science, Office of Basic Energy Sciences under Award Number DE-SC0021966. Work on the glycol-based side-chains was additionally supported by the Arnold and Mabel Beckman Foundation through a Beckman Young Investigator Award. P.H.L. and L.B.Z. were supported in part by the state of Washington through graduate fellowships from the University of Washington Clean Energy Institute. The authors acknowledge the use of instrumentation at the following shared facilities: the Washington Research Training Testbeds, a facility operated by the University of Washington Clean Energy Institute; the Molecular Analysis Facility, a National Nanotechnology Coordinated Infrastructure (NNCI) site at the University of Washington, which is supported in part by funds from the National Science Foundation (awards NNCI-2025489, NNCI-15421010), the Molecular Engineering & Sciences Institute, and the Clean Energy Institute; and the University of Washington Department of Chemistry. The NMR facility at the UW Department of Chemistry is supported by NIH Award Number S10OD030224-01A1. Finally, we gratefully acknowledge the W. M. Keck Microscopy Center and the Keck Center Manager, Dr. Nathaniel Peters for assistance in collecting optical microscopy data.

References.

(1) Bong, D. T.; Clark, T. D.; Granja, J. R.; Ghadiri, M. R. Self-Assembling Organic Nanotubes. *Angew. Chem. Int. Ed.* **2001**, *40* (6), 988–1011. https://doi.org/10.1002/1521-3773(20010316)40:6<988::AID-ANIE9880>3.0.CO;2-N.
(2) Balbo Block, M. A.; Kaiser, C.; Khan, A.; Hecht, S. Discrete Organic Nanotubes Based on a Combination of Covalent and Non-Covalent Approaches. In *Functional Molecular Nanostructures*; Schlüter, A. D., Ed.; Topics in Current Chemistry; Springer Berlin Heidelberg: Berlin, Heidelberg, 2005; Vol. 245, pp 89–150. https://doi.org/10.1007/b98167.
(3) Gong, B.; Shao, Z. Self-Assembling Organic Nanotubes with Precisely Defined, Sub-Nanometer Pores: Formation and Mass Transport Characteristics. *Acc. Chem. Res.* **2013**, *46* (12), 2856–2866. https://doi.org/10.1021/ar400030e.
(4) Strauss, M. J.; Evans, A. M.; Roesner, E. K.; Monsky, R. J.; Bardot, M. I.; Dichtel, W. R. Divergent Nanotube Synthesis through Reversible Macrocycle Assembly. *Acc. Mater. Res.* **2022**, *3* (9), 935–947. https://doi.org/10.1021/accountsmr.2c00062.
(5) Talukdar, D.; Kumar, J. M.; Gole, B. Self-Assembled Macrocycles: Design Strategies and Emerging Functions. *Crystal Growth & Design* **2023**, *23* (11), 7582–7611. https://doi.org/10.1021/acs.cgd.3c00677.
(6) Itoh, Y.; Chen, S.; Hirahara, R.; Konda, T.; Aoki, T.; Ueda, T.; Shimada, I.; Cannon, J. J.; Shao, C.; Shiomi, J.; Tabata, K. V.; Noji, H.; Sato, K.; Aida, T. Ultrafast Water Permeation through Nanochannels with a Densely Fluorous Interior Surface. *Science* **2022**, *376* (6594), 738–743. https://doi.org/10.1126/science.abd0966.
(7) Jiang, Z.; Dong, R.; Evans, A. M.; Biere, N.; Ebrahim, M. A.; Li, S.; Anselmetti, D.; Dichtel, W. R.; Livingston, A. G. Aligned Macrocycle Pores in Ultrathin Films for Accurate Molecular Sieving. *Nature* **2022**, *609* (7925), 58–64. https://doi.org/10.1038/s41586-022-05032-1.
(8) Zhang, G.; Lin, W.; Huang, F.; Sessler, J.; Khashab, N. M. Industrial Separation Challenges: How Does Supramolecular Chemistry Help? *J. Am. Chem. Soc.* **2023**, *145* (35), 19143–19163. https://doi.org/10.1021/jacs.3c06175.
(9) Helsel, A. J.; Brown, A. L.; Yamato, K.; Feng, W.; Yuan, L.; Clements, A. J.; Harding, S. V.; Szabo, G.; Shao, Z.; Gong, B. Highly Conducting Transmembrane Pores Formed by Aromatic Oligoamide Macrocycles. *J. Am. Chem. Soc.* **2008**, *130* (47), 15784–15785. https://doi.org/10.1021/ja807078y.
(10) Zhou, X.; Liu, G.; Yamato, K.; Shen, Y.; Cheng, R.; Wei, X.; Bai, W.; Gao, Y.; Li, H.; Liu, Y.; Liu, F.; Czajkowsky, D. M.; Wang, J.; Dabney, M. J.; Cai, Z.; Hu, J.; Bright, F. V.; He, L.; Zeng, X. C.; Shao, Z.; Gong, B. Self-Assembling Subnanometer Pores with Unusual Mass-Transport Properties. *Nat Commun* **2012**, *3* (1), 949. https://doi.org/10.1038/ncomms1949.
(11) Strauss, M. J.; Hwang, I.; Evans, A. M.; Natraj, A.; Aguilar-Enriquez, X.; Castano, I.; Roesner, E. K.; Choi, J. W.; Dichtel, W. R. Lithium-Conducting Self-Assembled Organic Nanotubes. *J. Am. Chem. Soc.* **2021**, *143* (42), 17655–17665. https://doi.org/10.1021/jacs.1c08058.
(12) Strauss, M. J.; Jia, M.; Evans, A. M.; Castano, I.; Li, R. L.; Aguilar-Enriquez, X.; Roesner, E. K.; Swartz, J. L.; Chavez, A. D.; Enciso, A. E.; Stoddart, J. F.; Rolandi, M.; Dichtel, W. R. Diverse Proton-Conducting Nanotubes via a Tandem Macrocyclization and Assembly Strategy. *J. Am. Chem. Soc.* **2021**, *143* (21), 8145–8153. https://doi.org/10.1021/jacs.1c02789.

(13) Yang, J.; Dewal, M. B.; Shimizu, L. S. Self-Assembling Bisurea Macrocycles Used as an Organic Zeolite for a Highly Stereoselective Photodimerization of 2-Cyclohexenone. *J. Am. Chem. Soc.* **2006**, *128* (25), 8122–8123. https://doi.org/10.1021/ja062337s.
(14) Islam, M. F.; Adame-Ramirez, E.; Williams, E. R.; Kittikhunnatham, P.; Wijesekera, A.; Zhang, S.; Ge, T.; Stefik, M.; Smith, M. D.; Pellechia, P. J.; Greytak, A. B.; Shimizu, L. S. Inclusion Polymerization of Pyrrole and Ethylenedioxythiophene in Assembled Triphenylamine *Bis* -Urea Macrocycles. *Macromolecules* **2022**, *55* (24), 11013–11022. https://doi.org/10.1021/acs.macromol.2c02042.
(15) Norikane, Y.; Hirai, Y.; Yoshida, M. Photoinduced Isothermal Phase Transitions of Liquid-Crystalline Macrocyclic Azobenzenes. *Chem. Commun.* **2011**, *47* (6), 1770–1772. https://doi.org/10.1039/C0CC04052E.
(16) Sun, C.; Shen, M.; Chavez, A. D.; Evans, A. M.; Liu, X.; Harutyunyan, B.; Flanders, N. C.; Hersam, M. C.; Bedzyk, M. J.; Olvera De La Cruz, M.; Dichtel, W. R. High Aspect Ratio Nanotubes Assembled from Macrocyclic Iminium Salts. *Proc. Natl. Acad. Sci. U.S.A.* **2018**, *115* (36), 8883–8888. https://doi.org/10.1073/pnas.1809383115.
(17) Zasada, L. B.; Guio, L.; Kamin, A. A.; Dhakal, D.; Monahan, M.; Seidler, G. T.; Luscombe, C. K.; Xiao, D. J. Conjugated Metal–Organic Macrocycles: Synthesis, Characterization, and Electrical Conductivity. *J. Am. Chem. Soc.* **2022**, *144* (10), 4515–4521. https://doi.org/10.1021/jacs.1c12596.
(18) Brunsveld, L.; Folmer, B. J. B.; Meijer, E. W.; Sijbesma, R. P. Supramolecular Polymers. *Chem. Rev.* **2001**, *101* (12), 4071–4098. https://doi.org/10.1021/cr990125q.
(19) De Greef, T. F. A.; Smulders, M. M. J.; Wolffs, M.; Schenning, A. P. H. J.; Sijbesma, R. P.; Meijer, E. W. Supramolecular Polymerization. *Chem. Rev.* **2009**, *109* (11), 5687–5754. https://doi.org/10.1021/cr900181u.
(20) Aida, T.; Meijer, E. W.; Stupp, S. I. Functional Supramolecular Polymers. *Science* **2012**, *335* (6070), 813–817. https://doi.org/10.1126/science.1205962.
(21) Smith, M. K.; Powers-Riggs, N. E.; Northrop, B. H. Rational Synthesis of Bis(Hexyloxy)-Tetra(Hydroxy)-Triphenylenes and Their Derivatives. *RSC Adv.* **2014**, *4* (72), 38281–38292. https://doi.org/10.1039/C4RA06503D.
(22) Giovannitti, A.; Sbircea, D.-T.; Inal, S.; Nielsen, C. B.; Bandiello, E.; Hanifi, D. A.; Sessolo, M.; Malliaras, G. G.; McCulloch, I.; Rivnay, J. Controlling the Mode of Operation of Organic Transistors through Side-Chain Engineering. *Proc. Natl. Acad. Sci. U.S.A.* **2016**, *113* (43), 12017–12022. https://doi.org/10.1073/pnas.1608780113.
(23) Nielsen, C. B.; Giovannitti, A.; Sbircea, D.-T.; Bandiello, E.; Niazi, M. R.; Hanifi, D. A.; Sessolo, M.; Amassian, A.; Malliaras, G. G.; Rivnay, J.; McCulloch, I. Molecular Design of Semiconducting Polymers for High-Performance Organic Electrochemical Transistors. *J. Am. Chem. Soc.* **2016**, *138* (32), 10252–10259. https://doi.org/10.1021/jacs.6b05280.
(24) Moser, M.; Ponder, J. F.; Wadsworth, A.; Giovannitti, A.; McCulloch, I. Materials in Organic Electrochemical Transistors for Bioelectronic Applications: Past, Present, and Future. *Adv Funct Materials* **2019**, *29* (21), 1807033. https://doi.org/10.1002/adfm.201807033.
(25) Paulsen, B. D.; Tybrandt, K.; Stavrinidou, E.; Rivnay, J. Organic Mixed Ionic–Electronic Conductors. *Nat. Mater.* **2020**, *19* (1), 13–26. https://doi.org/10.1038/s41563-019-0435-z.
(26) Moro, S.; Siemons, N.; Drury, O.; Warr, D. A.; Moriarty, T. A.; Perdigão, L. M. A.; Pearce, D.; Moser, M.; Hallani, R. K.; Parker, J.; McCulloch, I.; Frost, J. M.; Nelson, J.; Costantini, G. The Effect of Glycol Side Chains on the Assembly and Microstructure of Conjugated

Polymers. *ACS Nano* **2022**, *16* (12), 21303–21314. https://doi.org/10.1021/acsnano.2c09464.
(27) Zhong, Y.; Yang, Y.; Shen, Y.; Xu, W.; Wang, Q.; Connor, A. L.; Zhou, X.; He, L.; Zeng, X. C.; Shao, Z.; Lu, Z.; Gong, B. Enforced Tubular Assembly of Electronically Different Hexakis(*m* -Phenylene Ethynylene) Macrocycles: Persistent Columnar Stacking Driven by Multiple Hydrogen-Bonding Interactions. *J. Am. Chem. Soc.* **2017**, *139* (44), 15950–15957. https://doi.org/10.1021/jacs.7b09647.
(28) Yu, P.; Zhen, Y.; Dong, H.; Hu, W. Crystal Engineering of Organic Optoelectronic Materials. *Chem* **2019**, *5* (11), 2814–2853. https://doi.org/10.1016/j.chempr.2019.08.019.
(29) Crist, B.; Schultz, J. M. Polymer Spherulites: A Critical Review. *Progress in Polymer Science* **2016**, *56*, 1–63. https://doi.org/10.1016/j.progpolymsci.2015.11.006.
(30) Hmadeh, M.; Lu, Z.; Liu, Z.; Gándara, F.; Furukawa, H.; Wan, S.; Augustyn, V.; Chang, R.; Liao, L.; Zhou, F.; Perre, E.; Ozolins, V.; Suenaga, K.; Duan, X.; Dunn, B.; Yamamto, Y.; Terasaki, O.; Yaghi, O. M. New Porous Crystals of Extended Metal-Catecholates. *Chem. Mater.* **2012**, *24* (18), 3511–3513. https://doi.org/10.1021/cm301194a.
(31) Day, R. W.; Bediako, D. K.; Rezaee, M.; Parent, L. R.; Skorupskii, G.; Arguilla, M. Q.; Hendon, C. H.; Stassen, I.; Gianneschi, N. C.; Kim, P.; Dincă, M. Single Crystals of Electrically Conductive Two-Dimensional Metal–Organic Frameworks: Structural and Electrical Transport Properties. *ACS Cent. Sci.* **2019**, *5* (12), 1959–1964. https://doi.org/10.1021/acscentsci.9b01006.
(32) Snook, K. M.; Zasada, L. B.; Chehada, D.; Xiao, D. J. Oxidative Control over the Morphology of $Cu_3(HHTP)_2$, a 2D Conductive Metal–Organic Framework. *Chem. Sci.* **2022**, *13* (35), 10472–10478. https://doi.org/10.1039/D2SC03648G.